

## Research Article

# Modeling Based Characterization of Thermorheological Properties of Polyurethane ESTANE™

Ehsan Ghobadi,<sup>1</sup> Rakulan Sivanesapillai,<sup>1</sup> Jana Musialak,<sup>2</sup> and Holger Steeb<sup>1,2</sup>

<sup>1</sup>*Institute of Mechanics (CE), University of Stuttgart, Pfaffenwaldring 7, 70569 Stuttgart, Germany*

<sup>2</sup>*Institute of Mechanics, Faculty of Civil and Environmental Engineering, Ruhr-University Bochum, Universitätsstraße 150, 44801 Bochum, Germany*

Correspondence should be addressed to Ehsan Ghobadi; [ehsan.ghobadi@mechbau.uni-stuttgart.de](mailto:ehsan.ghobadi@mechbau.uni-stuttgart.de)

Received 19 March 2016; Revised 7 June 2016; Accepted 22 June 2016

Academic Editor: Kai Chen

Copyright © 2016 Ehsan Ghobadi et al. This is an open access article distributed under the Creative Commons Attribution License, which permits unrestricted use, distribution, and reproduction in any medium, provided the original work is properly cited.

Shape-Memory Polymers (SMPs) have the ability to be deformed and memorize this deformation until an external activation stimulus (e.g., heat) is applied. Therefore, they have attracted great interest in many areas, especially for applications where reconfigurable structures are required (e.g., Shape-Memory (SM) stents or micro air vehicles). Nevertheless, prior to technical application, the effective thermomechanical behavior of SMPs must be thoroughly understood. In the current contribution, an assessment of thermorheological properties of the commercially available polyurethane system ESTANE is presented. Thermorheological properties were investigated using Dynamic Mechanical Thermal Analysis (DMTA) and complementary uniaxial stress relaxation experiments. Upon material parameter optimization, a finite viscoelastic and incompressible material model was used to model experimentally observed viscoelastic properties.

## 1. Introduction

Shape-Changing Materials (SCMs) together with Shape-Memory Materials (SMMs) are two kinds of smart materials with the ability to vary their shape upon being exposed to activation stimuli [1]. Typical stimuli for activating SMMs (or Shape-Memory Polymers, SMPs) consist of temperature (including both cooling and heating either directly or indirectly, e.g., inductive or resistive heating), chemicals, and light [1, 2]. In contrast to SCMs (or Shape-Changing Polymers, SCPs), which can preserve a deformed shape only as long as an external stimulus is applied, SMMs (or SMPs) can be deformed and fixed to several different forms and recover their reference shape when the activation stimulus is triggered.

Depending on environmental and boundary conditions, for example, temperature, and the applied stimulus, a polymer could be either SMP or SCP [3]. In the case of heat as the activation stimulus, the SMP is called thermally induced SMP. The capability of a material to temporarily preserve a deformed shape and recover the undeformed reference shape upon triggering using an external activation stimulus

is known as the Shape-Memory-Effect (SME). In fact, there are two types of thermoresponsive SME. The first type is responsive with respect to heating, which is an almost intrinsic feature of all polymers, and the other one is cooling responsive, which is only limited to a couple of specially designed polymeric materials [3]. Compared to other smart materials, several properties of SMPs, for example, their glass transition temperature ( $T_g$ ) or dynamic modulus, can be easily tailored to meet specific requirements. Therefore, they have drawn much attention and are intensively used in different applications [4].

Essential requisites for a polymer to exhibit the SME are an appropriate polymer structure and morphology together with the use of appropriate processing and programming methods [2, 4]. In the so-called uniaxial Shape-Memory Creation Procedure (SMCP) [5, 6], the polymer is heated to a temperature ( $T_{\text{prog}}$ ) which is normally higher than its transition temperature ( $T_g$  or melting temperature  $T_m$ ). Afterwards, it is deformed in a stress-controlled or strain-controlled process to a prescribed stretch ratio  $\lambda_1$  in loading direction  $\mathbf{e}_1$ . Subsequently, the polymer is cooled down to a temperature below the transition temperature ( $T_{\text{low}}$ ) in order

to solidify the switching domains resulting in mechanical fixation of the deformed shape upon stress unloading. For activation of the SME, the programmed shape should be excited, for example, by heating to a temperature above the transition temperature ( $T_{sw}$ ) [7].

Two important characteristics for quantification of SME are shape fixity ratio ( $R_f$ ) and shape recovery ratio ( $R_r$ ), which are usually quantified by cyclic thermomechanical investigations under uniaxial (biaxial) tension or compression or even bending experiments. Macroscopically, shape fixation is the extent up to which a deformation can be fixed after programming and shape recovery is the recoverability of the sample after being heated [8].

Characterization of SME requires investigations on thermomechanical and rheological behavior of the polymeric system through various modeling and experimental studies [9–13]. Generally, two different phenomenological modeling approaches can be used to model the mechanism of SME. The first model is called Standard-Linear-Solid (SLS) [14–16] which requires phenomenological constitutive relations for the temperature-dependence of the material properties. In recent years, such models have been well established and intensively discussed in literature; compare [17–21]. Although these models provide insight into the shape recovery behavior, they have limited predictive capabilities, and their applications are mostly limited to one-dimensional problems. Therefore, recent works have shifted towards more physical descriptions of the underlying (Shape-Memory) SM mechanisms [22]. A further set of modeling approaches explicitly accounts for the underlying morphology of the polymer. These models are known as phase transition or frozen volume fraction approaches [23–25] and describe the transition of the dominant microscopic deformation mechanism from entropy-driven conformational chain rearrangements at high temperatures to molecular deformations corresponding to an internal energy change at low temperatures. Here, amorphous polymers are considered as two-phase materials composed of frozen and active parts such that the total strain could be represented as the sum of two contributions from respective volume fractions [26]. Although these models deliver good results with comparatively small number of parameters, still limited perception about the underlying physics could be achieved. Therefore, for design and evaluation of mechanical components with complex geometries under realistic loading and environmental conditions, prior to any modeling activity, comprehensive experimental studies on thermal and mechanical properties over a wide temperature, time, and strain range are required [13]. To this end, an extensive thermomechanical analysis of a SM-polyurethane, commercially available under the name ESTANE, is first performed. By applying the theory of finite viscoelasticity and based on the rheological results achieved here, the constitutive viscoelastic behavior of ESTANE is represented by a generalized Maxwell-Zener model.

## 2. Material and Methods

**2.1. Material.** In the present contribution, aliphatic SM-polyurethane ESTANE ETE75DT3 NAT022 granulates (Lubrizol,

Ovele Westerlo, Belgium) have been processed using an injection molding machine (Arburg Allrounder 270M 500-210, Lossburg, Germany). Sample preparation and preprocessing steps have been described in detail in [27].

For quantitative characterization of the polymer, two complementary sets of experiments have been performed: The Dynamic Mechanical Thermal Analysis (DMTA) and quasistatic stress relaxation experiments.

**2.2. Thermorheological Characterization.** To determine the time-temperature-dependent viscoelastic properties, DMTA tests in torsion mode were performed using rectangular samples with dimensions of  $W \times H \times L$ : 2 mm  $\times$  10 mm  $\times$  50 mm. Here, DMTA experiments were performed with a stress-controlled rheometer with integrated Peltier-based temperature chamber (Anton Paar Physica MCR 301 plus CTD 180, Graz, Austria). The isothermal scans were carried out at specially chosen temperature set points in the range of 20 to 90°C. For frequencies from 0.01 up to 100 rad·s<sup>-1</sup>, harmonic twist rotations were applied with maximum amplitudes of 0.2% while resulting torques as well as phase lags were monitored. Subsequently, RheoPlus software [28] was used to calculate the corresponding magnitude of complex shear modulus  $|G^*|$ , storage modulus  $G'$ , loss modulus  $G''$ , and loss factor  $\tan \delta$ , which are related to each other according to the following relations [29]:

$$\begin{aligned} |G^*| &= \sqrt{G'^2 + G''^2}, \\ \tan \delta &= \frac{G''}{G'}. \end{aligned} \quad (1)$$

The dynamic shear modulus  $G^* = G' + iG''$  is the appropriate constitutive measure to evaluate stresses relaxation during strain-controlled experiments. Equivalently, in stress-controlled experiments, the complex shear compliance  $J^*$  determines strain retardation where

$$\begin{aligned} |J^*| &= \frac{1}{|G^*|}, \\ J' &= |J^*| \cos \delta, \\ J'' &= |J^*| \sin \delta. \end{aligned} \quad (2)$$

Here,  $J'$  represents the storage compliance and  $J''$  the loss compliance. Finally, for adequate thermorheological characterization of ESTANE, the (complex) dynamic viscosity was computed. The in-phase viscosity  $\eta'$  and out-of-phase viscosity  $\eta''$  as well as complex viscosity  $|\eta^*|$  are related to the loss and storage moduli in terms of

$$\begin{aligned} \eta' &= \frac{G''}{\omega}, \\ \eta'' &= \frac{G'}{\omega}, \\ |\eta^*| &= \frac{|G^*|}{\omega}, \end{aligned} \quad (3)$$

where  $\omega$  is the frequency.

**2.3. Stress Relaxation Experiments.** For quasistatic relaxation experiments, ESTANE plates were punched to dumbbell specimens of type 5A according to DIN EN ISO 527-2 ( $W \times H \times L$ : 2 mm  $\times$  4 mm  $\times$  75 mm). Uniaxial stretching and relaxation experiments were performed on a spindle-driven testing machine (Schenck Trebel RM50, New York, USA) with a stretching and compression capacity of  $\pm 500$  N. The machine was equipped with a heating chamber of type Fresenberger TK18.400.100 (Wipperfurth, Germany) attached to a PID temperature controller (Eurotherm 3508, Limburg, Germany) so that temperatures in the range of  $-100$  to  $400^\circ\text{C}$  could be adjusted and kept constant with a precision of  $\pm 1^\circ\text{C}$ .

For stress relaxation experiments in displacement driven control mode, all specimens were pneumatically fixed along their stretching axis and heated up with a rate of  $3^\circ\text{C}\cdot\text{min}^{-1}$  to a temperature  $T_{\text{prog}}$  which was equilibrated for at least 10 min. Afterwards, the specimens were deformed with a strain rate of  $0.005\text{ s}^{-1}$  from their initial length  $L$  to a new length  $l$  corresponding to a local uniaxial strain of about  $\varepsilon = (l - L)/L = 10\%$ . This uniaxial stretch  $\lambda = l/L = 1.1$  was kept constant for at least 60 min. At different temperatures  $T_{\text{prog}}$  ranging from  $10^\circ\text{C}$  up to  $80^\circ\text{C}$ , the decay of stress over time was monitored. Considering a linear viscoelastic behavior for ESTANE, the total stress will ultimately reach an equilibrium stress following the decay of multiple superimposed relaxation processes as long as no viscous flow occurs. It is worth mentioning that all experiments were repeated two times to improve confidence.

**2.4. Thermal Expansion Experiments.** To determine the Coefficient of Thermal Expansion (CTE), two different experiments were conducted. The first procedure was performed with the same spindle-driven machine as used for the relaxation experiments. Here the samples were heated while a force controlled loop kept a tensile force of approximately 0.5 N constant using the feedback signals of a load cell that was attached to the moving upper clamp and an actuator. The upper clamp displacement during heating was tracked and, assuming a homogeneous deformation, subsequently used to determine the sample deformation. The corresponding temperature (from 10 to  $140^\circ\text{C}$ ) versus stretch data was used to compute the Coefficients of Thermal Expansion.

In addition to this, the same rheometer which was used for DMTA experiments was applied as an alternative method for stress-controlled CTE-measurement. In equivalence to the above approach, a tensile force of 0.5 N was controlled to be constant while heating the samples from 10 to  $140^\circ\text{C}$ . In contrast to the uniaxial spindle-driven testing machine the advantage of the rheometer apparatus is the use of a high-resolution load cell with an accuracy of 0.005 N.

### 3. Results and Discussion

#### 3.1. Characterization

**3.1.1. Determination of Thermal Expansion.** A subtle discontinuity in the CTE, which otherwise exhibits a linear temperature dependency, is observed for both rheometer

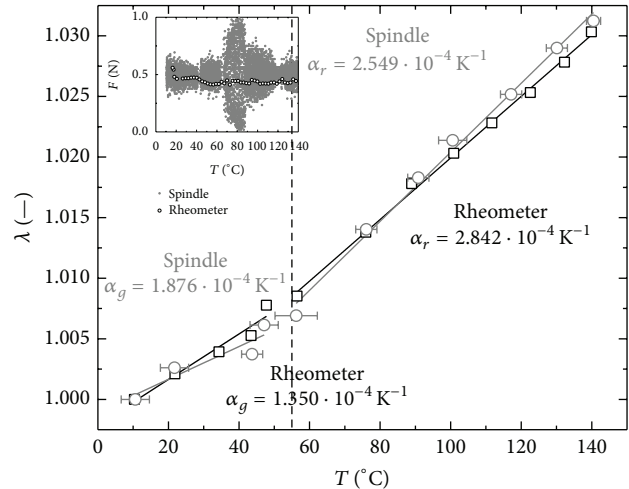


FIGURE 1: Thermal expansion during heating while applying constant tensile force of 0.5 N.

and spindle-driven testing procedures. The corresponding data points and best fitting linear regressions are depicted in Figure 1. The tensile force which was controlled during heating is plotted in the inset to Figure 1. Pronounced fluctuations in the applied tensile force around  $T_g$  suggest that quantitative measurement of CTE is impeded for the less accurate spindle-driven testing procedure. The force controlling mechanism was more accurate during rheometer testing which we attribute to higher accuracy of the load sensor. The magnitudes of elongation are furthermore found to be distinctly small such that data acquisition errors need to be considered. The corresponding magnitudes of uncertainty are illustrated by means of error bars and found to be comparatively high at low temperatures. The subscripts “g” and “r” indicate the regions of glass-like and rubbery behavior, respectively. Below  $T_g$ , the CTE is less pronounced which produces a kink in the  $\lambda$ - $T$  curve. The discontinuity of linear thermal expansion, which we attribute to glass transition, is found at  $T_g \approx 55^\circ\text{C}$ . This coincides with previously reported results in [27, 30].

**3.2. Dynamic Thermomechanical Experiments.** Aim of the (cyclic/harmonic) amplitude sweeps is to determine a linear regime where effective properties are independent of the (shear strain) amplitude. Therefore, DMTA amplitude sweep tests, where the strain amplitude increases incrementally with fixed frequency, are used to determine the linear viscoelastic region (LVR). Within the LVR the viscoelastic response of the polymer is independent of the amplitude of deformation such that constitutive nonlinearities and plasticity effects can be excluded. In Figure 2, the variations of storage and loss moduli with strain amplitude  $\gamma_0$  at different temperatures (0, 40, and  $80^\circ\text{C}$ ) are depicted. In the low temperature regime ( $T = 0^\circ\text{C}$ , Figure 2, black dots), the mechanical response ( $G'$ ) is dominated by the hard segment phase. It could be observed that  $G'$  and  $G''$  is hardly amplitude dependent within  $0.03\% < \gamma < 1\%$  and no hint for any plastic behavior is observed. In the high temperature regime ( $T = 80^\circ\text{C}$ , Figure 2,

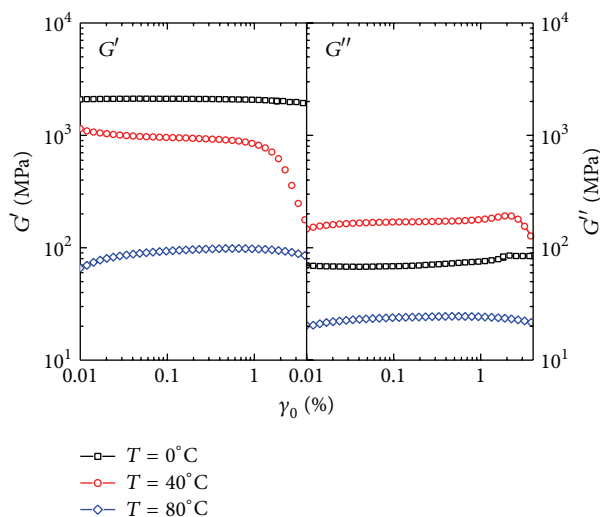


FIGURE 2: Amplitude sweep test at different temperatures.

blue diamonds), the mechanical properties are determined by the soft segments. In this graph, the linear viscoelastic region can be identified as a pronounced plateau. For shear amplitudes within the range  $0.03\% < \gamma < 1\%$ , the storage and loss moduli remain almost constant. This is a fairly broad LVR when compared to previously reported LVRs [29]. For shear amplitudes smaller than  $0.03\%$ , the decrease in the experimental signal-to-noise ratio results in an artificial deviation of moduli from the LVR plateau.

Upon identifying the appropriate strain amplitude range, storage and loss moduli have been measured using temperature sweeps as shown in Figure 3(a). As can be seen, DMTA in temperature sweep mode gives intriguing information about structural properties of ESTANE. It is shown that the storage modulus  $G'$  decreases gradually with temperature until the glass transition region is reached. The plotted behavior is typical for physically cross-linked block copolymers [31]. The inflection point of the  $G'$ - $T$ -graph determines  $T_g$  of the sample. This point shifts to a higher temperature as frequency increases.  $T_g$  of SM-ESTANE was measured to be approximately  $55^\circ\text{C}$ , which is in agreement with previously reported results [30]. Interestingly, the temperature sweep tests of SM-ESTANE scanned at different frequencies indicates that the reduction of  $G'$  is less pronounced at higher frequencies than at lower ones. Moreover, the storage modulus decreases until it reaches a minimum. This is more considerable for samples under lower tested frequencies. This minimum, located at temperatures higher than  $T_g$ , is characteristic for another relaxation inside the polymer chains due to molecular heterogeneities of the specimen. Samples under higher frequencies have less or not enough time to show this relaxation. An inverse temperature sweep test with the same frequency proves that this observation is almost not repeatable.

The loss modulus  $G''$  shows a different behavior.  $G''$ - $T$ -plot has also a nonmonotonic form. The curves increase with increasing temperature until  $T_g$  is attained and decrease slowly at higher temperatures. Moreover, at higher frequencies the loss modulus takes higher values. The maximum of

$G''$ - $T$ -graph is interpreted as  $T_g$  of the sample. Likewise, a minimum at  $T > T_g$ , characteristic for heterogeneities of the sample, is perceptible.

Moreover, in addition to storage and loss moduli, storage and loss compliance are plotted in Figure 3(b). As can be seen, the loss and storage compliance show a nonuniform behavior and obviously are in an almost opposite form in comparison with the loss and storage moduli. The storage compliance  $J'$  increases first gradually with respect to temperature until it reaches a maximum. The plotted loss compliance as a function of temperature for different frequencies has also a monotonic shape. It decreases with temperature until  $T_g$  is reached and then increases with higher slopes up to the second relaxation temperature.

In addition to this, the results of dynamic and out-of-phase viscosities as a function of temperature are plotted in Figure 4. Again, a nonmonotonic behavior can be observed for these properties and a stronger frequency dependence than that of moduli and compliance is obvious. It can be concluded that at higher frequencies the material shows more internal energy dominated glassy behavior, whereby at decreasing frequency a transition to a nearly entropic rubbery state is surveyed. This is because of the fact that at higher frequencies polymer chains absorb energy much better than at lower frequencies.

As shown in Figure 5, the temperature dependency of storage and loss moduli exhibit weak sensitivity with respect to heating rate  $\xi$ , which was varied in the range from 0.25 to  $2^\circ\text{C}\cdot\text{min}^{-1}$  during temperature sweeps. Below  $T_g$ , the storage modulus does not noticeably change with temperature and a smooth decreasing trend is observed. ESTANE demonstrates therefore a linear elastic behavior in this region. In the region around  $T_g$ , a harsh fall of storage modulus is observed. In this range, a pronounced difference can be observed for different heating rates. For higher heating rates, the storage modulus exhibits a global minimum at around  $T_g$ . This could be attributed to the fact that for higher heating rates, the kinetic energy of polymer chains increases noticeably resulting in a bigger free volume inside the polymer matrix. This volume expansion obtains the needed energy and space for chain movements in a defined time scale leading to an extreme subsidence of energy. However, after this range, the polymer chains resist to stresses due to physical cross-links and chain entanglements. Finally, one can conclude that the changes of mechanical properties depend more strongly upon frequency or strain amplitudes rather than heating rates. Additionally, the results of loss factor (damping coefficient) are shown in Figure 6. The peak values and the temperatures regarding this maximum point are very well detectable. A small shift towards higher temperatures for  $\tan\delta$  is seen for higher heating rates. A similar behavior is also recorded in other thermal analyses such as TMA or DSC [32].

Rearrangement of chain sequences in polymeric systems leading to molecular relaxations accelerates at higher rates and elevated temperatures. This direct equivalence between time and temperature leads to the fact that the time over which these relaxations take place can be simply reiterated by conducting the experiment at higher temperatures and shifting the resulting data to lower frequencies. This treating

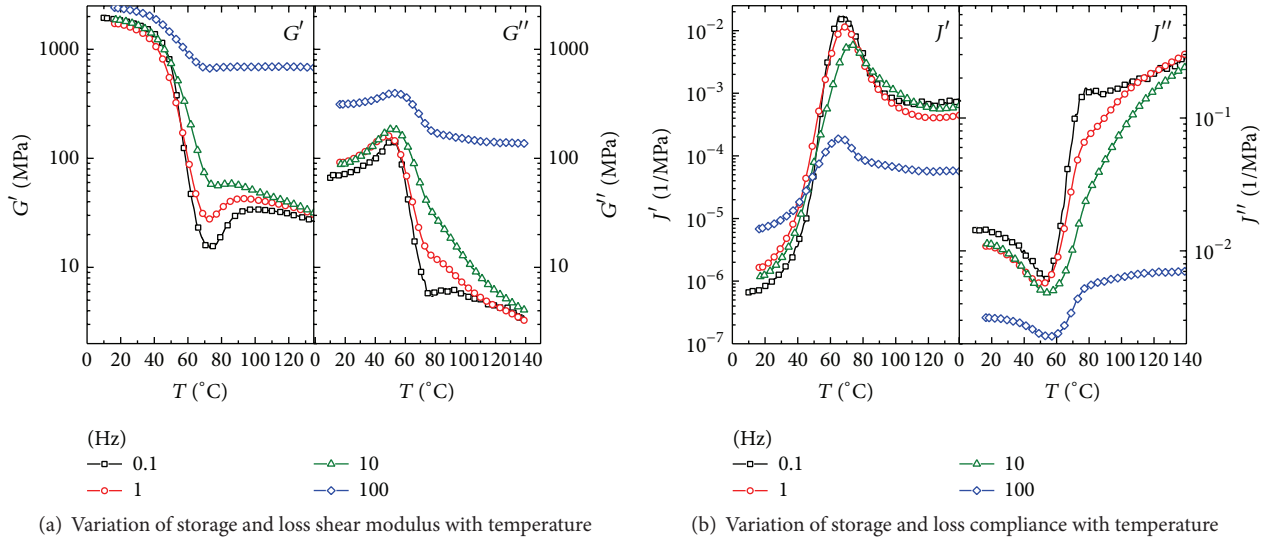


FIGURE 3: Temperature sweep tests at different frequencies.

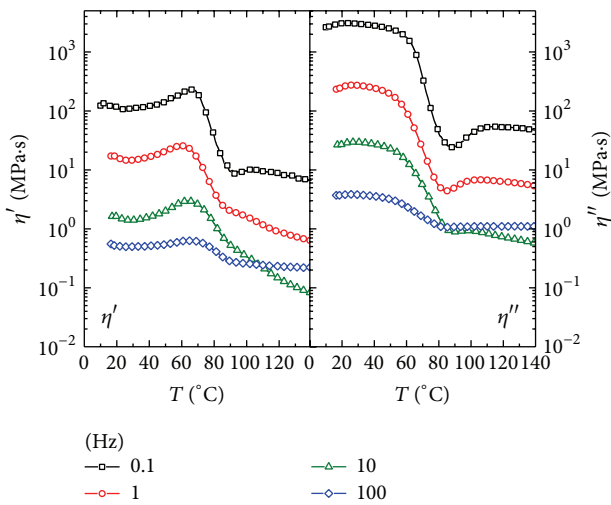


FIGURE 4: Temperature sweep tests at different frequencies: variation of dynamic and out-of-phase viscosities with temperature.

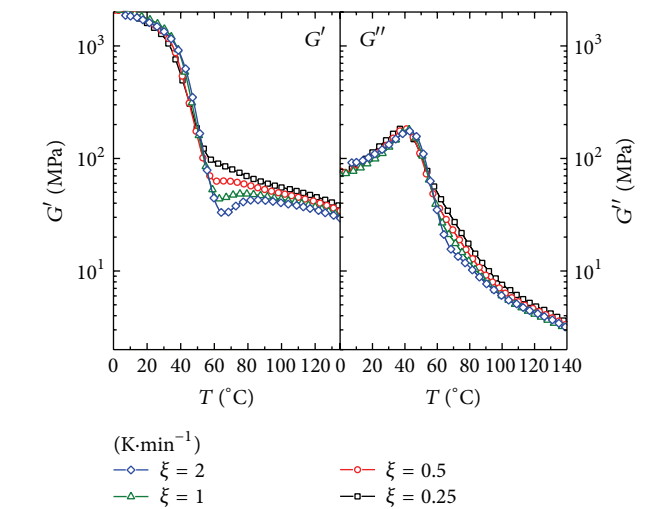


FIGURE 5: Temperature sweep tests with different heating rates: variation of storage and loss shear modulus with temperature.

of the results of dynamic experiments is called the Time-Temperature Superposition Principle [33] and can be used to produce a corresponding master curve of a polymer with which the material properties can be estimated for very long and not measurable time scales [29]. The horizontal shift factor values ( $a_T$ ) for linking the individual experimental data and producing the master curve can be obtained through the Williams-Landel-Ferry (WLF) equation [29]:

$$\log a_T = -\frac{C_1(T - T_r)}{C_2 + (T - T_r)}, \quad (4)$$

where  $C_1$  and  $C_2$  are empirical constants and  $T_r$  denotes the reference temperature.

Figure 7(a) demonstrates the experimentally obtained data of  $G'$  at different isothermal temperatures varying from 20°C to 70°C in the range of unreduced angular frequencies

$\omega$  from 0.1 to 100 rad·s<sup>-1</sup>. Complementary to this, obtained master curves of  $G'$  and  $G''$  are shown in Figure 7(b). Here,  $T_r$  is 50°C and  $C_1$  and  $C_2$  are found to be 8 and 18, respectively. As can be seen, the shift factor values of WLF equation and the chosen temperature increments lead to acceptable master curves from experimentally acquired data, revealing that ESTANE may be considered as thermorheologically simple. However, because of segmental and global heterogeneity, considering ESTANE as thermorheological complex [34, 35] would lead to even better master curves.

A very interesting inference, which can be concluded from the aspect of the resulting master curve, is the feature of the polymer system to show the SME. In the fact of the viscous nature of the system, which is essential to the shape-storage and recovery, one can deduce that the SME results only from the time-temperature-dependent property of the system and

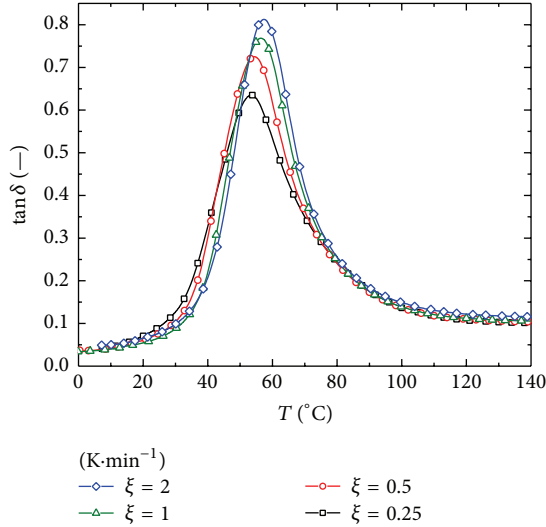


FIGURE 6: Temperature sweep tests with different heating rates: variation of loss factor with temperature.

its linear viscoelasticity [17]. By decreasing the temperature, the deformation is stored as viscous strain by a large increase in the viscosity or equivalently in the relaxation times (cf. Section 3.2.1). Additionally, the shape recovery would be achieved through viscous strain release owing to a decrease in viscosity by temperature elevation. Therefore, the shape fixation regardless of the cooling history can be estimated directly from the master curve through  $R_f = 1 - G_e/G_g$ , where  $G_e$  is the rubbery (at small frequencies) and  $G_g$  is the glassy (at high frequency) modulus.

**3.2.1. Constitutive Model.** A suitable constitutive framework for thermorheologically simple polymers is generalized Maxwell-Zener model [33] that is composed of a single neo-Hookean equilibrium element aligned in parallel to  $n$  nonequilibrium Maxwell elements. These nonequilibrium thermoviscoelastic elements describe distinct relaxation processes of the polymer [36]. In attempt to accurately represent the continuous viscoelastic spectrum as measured using DMTA,  $n = 19$  discrete nonequilibrium Maxwell elements are taken into account. The constitutive behavior of the  $j$ th Maxwell element is defined by the shear modulus  $G^j$  and the reduced relaxation time  $\tau_R^j$  and together they are referred to as Prony series coefficients. Both material parameters are optimized using the storage modulus master curve  $G'(\omega \cdot \alpha_T)$  for the reference temperature  $T_r$  as shown in Figure 7. We account for temperature dependency of the discrete relaxation processes by scaling  $\tau^j$  with the temperature shift factors  $a_T$  according to the Time-Temperature Superposition Principle (TTSP). As outlined in Section 3.2, the shift factors  $a_T$  have been found to obey the WLF relationship within the tested temperature range. For the present thermorheologically simple material, temperature dependency of the discrete relaxation processes takes the form  $\tau^j(T) = \tau_R^j \alpha_T(T)$ . The elastic shear modulus  $G_{eq}$  of the neo-Hookean equilibrium

TABLE 1: Generalized Maxwell model relaxation times  $\tau_R^j$  and associated shear moduli  $G^j$  for ESTANE.

$\tau_R^j$ [s]	$G^j$ [MPa]
$1.000 \times 10^{-9}$	$8.495 \times 10^1$
$5.995 \times 10^{-9}$	$7.954 \times 10^1$
$3.594 \times 10^{-8}$	$7.414 \times 10^1$
$2.154 \times 10^{-7}$	$6.874 \times 10^1$
$1.291 \times 10^{-6}$	$6.334 \times 10^1$
$7.743 \times 10^{-6}$	$5.794 \times 10^1$
$4.641 \times 10^{-5}$	$5.254 \times 10^1$
$2.782 \times 10^{-4}$	$4.713 \times 10^1$
$1.668 \times 10^{-3}$	$4.168 \times 10^1$
$1.000 \times 10^{-2}$	$3.602 \times 10^1$
$5.995 \times 10^{-2}$	$2.932 \times 10^1$
$3.594 \times 10^{-1}$	$2.106 \times 10^1$
$2.154 \times 10^0$	$1.399 \times 10^1$
$1.291 \times 10^1$	$9.998 \times 10^0$
$7.743 \times 10^1$	$8.412 \times 10^0$
$4.641 \times 10^2$	$7.613 \times 10^0$
$2.782 \times 10^3$	$6.331 \times 10^0$
$1.668 \times 10^4$	$4.651 \times 10^0$
$1.000 \times 10^5$	$2.823 \times 10^0$

element is evaluated in the limit  $\lim_{\omega \rightarrow 0} G'(\omega \cdot \alpha_T)$  as  $G_{eq} = 29$  MPa. Subsequently, the Prony coefficients  $G^j$  and  $\tau_R^j$  are optimized using the Tikhonov regularization method [37] such that the discrete representations of storage and loss moduli

$$G'(\omega, T) = G_{eq} + \sum_{j=1}^n G^j \frac{\omega^2 (\tau^j(T))^2}{1 + \omega^2 (\tau^j(T))^2}, \quad (5)$$

$$G''(\omega, T) = \sum_{j=1}^n G^j \frac{\omega \tau^j(T)}{1 + \omega^2 (\tau^j(T))^2}$$

adequately represent experimentally measured DMTA data. The best fitting Prony coefficients are listed in Table 1. The fitted storage and loss moduli are plotted in Figure 7 and found to accurately represent the dynamic material properties within the frequency and temperature range of interest.

**3.2.2. Modeling: Parameter Identification.** In this section the material parameter optimization techniques are discussed. According to the rheological properties presented here, the theory of finite viscoelasticity is used [38]. By considering homogeneous uniaxial deformations, the resulting constitutive model is reduced to a scalar equation entitled constitutive driver. Consistent with [39, 40], the total deformation gradient  $\mathbf{F} = \partial \mathbf{x} / \partial \mathbf{X} = F_{ij} \bar{\mathbf{e}}_i \otimes \bar{\mathbf{e}}_j$  can be decomposed into an elastic and inelastic part:  $\mathbf{F} = \mathbf{F}_e \cdot \mathbf{F}_i$ . For uniaxial tension

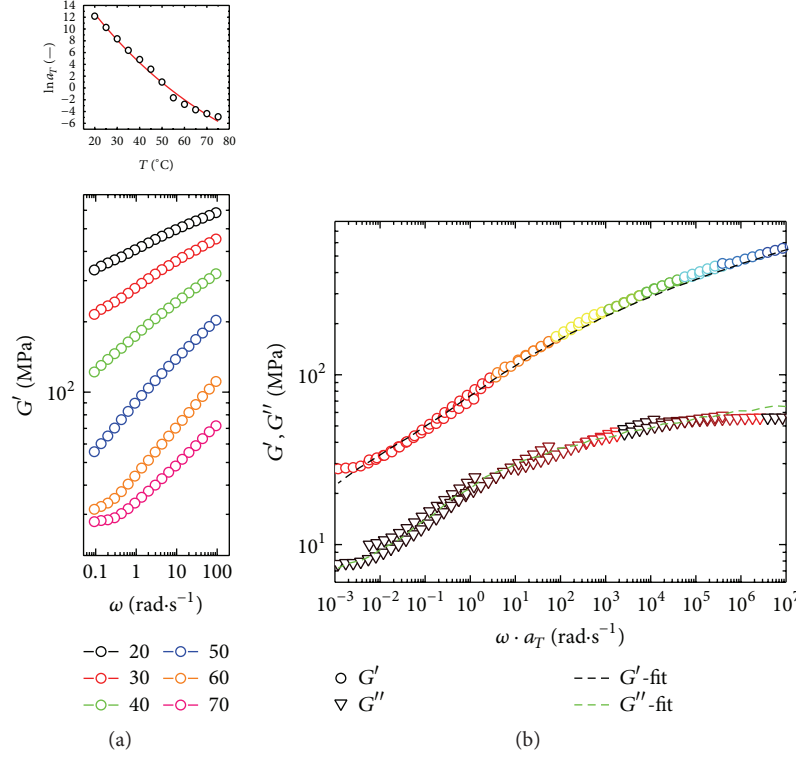


FIGURE 7: (a) Storage modulus as a function of angular frequency at different isothermal conditions obtained from DMTA experiments and (b) master curves of storage and loss moduli shifted to a reference temperature of  $T_r = 50^\circ\text{C}$ . The solid line in the insert shows the calculated shift factors obtained from WLF approximation.

of an incompressible material in  $\mathbf{e}_2$  direction, assuming an isotropic thermal expansion, one can write

$$\mathbf{F} = \begin{bmatrix} \frac{1}{\sqrt{\lambda}} & 0 & 0 \\ 0 & \lambda & 0 \\ 0 & 0 & \frac{1}{\sqrt{\lambda}} \end{bmatrix}, \quad (6)$$

where  $\lambda$  is the previously introduced stretch. Similarly, the stretch ratio of the  $j$ th Maxwell unit  $\lambda^j$  can be decomposed into  $\lambda^j = \lambda_e^j \lambda_i^j$ . A neo-Hookean strain energy function is taken into account for both, the equilibrium and nonequilibrium stresses. The resulting constitutive equation reads

$$\mathbf{T} = \mathbf{T}_{\text{eq}} + \mathbf{T}_{\text{neq}} = G_{\text{eq}} \mathbf{B} + \sum_{j=1}^n G^j \mathbf{B}_e^j - p \mathbf{I}, \quad (7)$$

where  $\mathbf{T}$ ,  $\mathbf{B} = \mathbf{F} \cdot \mathbf{F}^T$ , and  $\mathbf{B}_e^j = \mathbf{F}_e \cdot \mathbf{F}_e^T$  are the Cauchy stress tensor, the total left Cauchy-Green tensor, and the elastic left Cauchy-Green tensor of the  $j$ th Maxwell unit, respectively. The volumetric Lagrange parameter  $p$  in constitutive equation (7), which accounts for the incompressibility constraint and thus interpreted as a pressure, can be evaluated from the boundary condition. Since the material is stretched in just

one direction, the orthogonal directions are stress free. This means  $T_{11} = T_{33} = 0$ , which results in

$$T = G_{\text{eq}} \left( \lambda^2 - \frac{1}{\lambda} \right) + \sum_{j=1}^n G^j \left[ \frac{\lambda^2}{(\lambda_i^j)^2} - \frac{\lambda_i^j}{\lambda} \right]. \quad (8)$$

Using the relation above, the inelastic component  $\lambda_i^j$  can be replaced by  $\lambda^j / \lambda_e^j$ . The evolution of the inelastic right Cauchy-Green tensor  $\mathbf{C}_i^j$ , which takes the role of the internal variables reads in general [40]

$$\dot{\mathbf{C}}_i^j = \frac{2}{\tau^j(T)} \left[ \mathbf{C} - \frac{1}{3} \text{tr}(\mathbf{C} \cdot [\mathbf{C}_i^j]^{-1}) \mathbf{C}_i^j \right], \quad (9)$$

with the right Cauchy-Green tensor  $\mathbf{C} = \mathbf{F}^T \cdot \mathbf{F}$  and the inelastic right Cauchy-Green tensor of the  $j$ th Maxwell unit  $\mathbf{C}_i^j = (\mathbf{F}_i^j)^T \cdot \mathbf{F}_i^j$ .

For linearization of this equation we use the method described in [40]:

$$\dot{\mathbf{C}}_i^j = \frac{2}{\tau^j(T)} \left[ \mathbf{C} - \mathbf{C}_i^j \right]. \quad (10)$$

An alternative approach is constituted by Shutov et al. proposing a simple iteration scheme without linearization by an implicit integration procedure and a simple explicit update formula for unimodular deformations [41]. In view of the

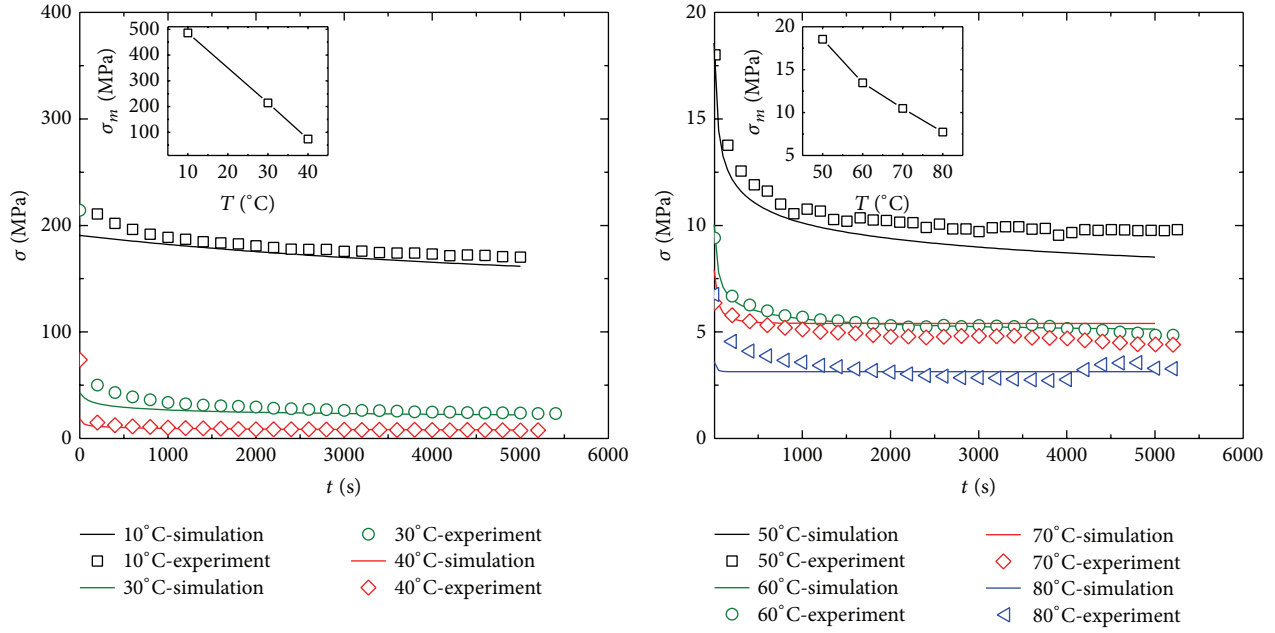


FIGURE 8: Temporal development of loading and stress relaxation experiments and their associated simulations under different isothermal conditions.

scalar constitutive driver, the inelastic stretch component  $\lambda_i^j$  takes the role of the internal variable. The corresponding linear evolution equation reads

$$\dot{\lambda}_i^j = \frac{1}{2\tau^j(T)} \left[ \frac{\lambda^2}{\lambda_i^j} - \lambda_i^j \right]. \quad (11)$$

The linearized evolution in (10) and (11) is only applicable to boundary value problems with small deformation rates. For these, large deviations with respect to the point of linearization  $\mathbf{C}_i^j = \mathbf{I}$  are not expected. Equation (11) can be solved by the implicit backward Euler procedure in time

$$\begin{aligned} \dot{\lambda} &\approx \frac{\lambda_i^j(t + \Delta t) - \lambda_i^j(t)}{\Delta t} \\ &= \frac{1}{2\tau^j(T)} \left[ \frac{\lambda^2(t + \Delta t)}{\lambda_i^j(t + \Delta t)} - \lambda_i^j(t + \Delta t) \right]. \end{aligned} \quad (12)$$

Equation (12) is reformulated into a root-finding problem for the updated inelastic stretch ratio of the  $j$ th Maxwell element, which is solved using a Newton-Raphson scheme. The corresponding residual form in the  $k$ th iteration reads

$$\begin{aligned} \mathfrak{R}^k &= \lambda_i^{j,k}(t + \Delta t) - \lambda_i^j(t) \\ &\quad - \frac{\Delta t}{2\tau^j(T)} \left[ \frac{\lambda^2(t + \Delta t)}{\lambda_i^{j,k}(t + \Delta t)} - \lambda_i^j(t + \Delta t) \right]. \end{aligned} \quad (13)$$

Every Newton-Raphson iteration needs a new tangent

$$\begin{aligned} \mathcal{H}^k &= \frac{\partial \mathfrak{R}}{\lambda_i^{j,k}(t + \Delta t)} \\ &= 1 + \frac{\Delta t}{2\tau^j(T)} \left[ 1 + \frac{(\lambda(t + \Delta t))^2}{(\lambda_i^j(t + \Delta t))^2} \right]. \end{aligned} \quad (14)$$

It is worth stating that the root-finding algorithm terminates when the residual function ( $\mathfrak{R}^k$ ) reaches the threshold value of  $10^8$ .

**3.2.3. Finite Deformation Modeling: Rheology-Based.** As shown before, Prony coefficients as well as the WLF constants have been determined for small deformations from frequency sweep DMTA experiments. The parameter identification is based on these results. Here for parameter validation, relaxation experiments described in Section 2.3 were used and compared to modeling results as obtained from the constitutive approach discussed in Section 3.2.

The stress relaxation experiments with ESTANE have been conducted at different temperatures ( $T_{\text{prog}} = 10, 30, 40, 50, 60, 70,$  and  $80^\circ\text{C}$ ). The typical stress relaxation curves and the appending simulated data of relaxations are depicted in Figure 8, once for temperature below  $T_g$  and once above it. Obviously, a pronounced peak maximum at  $t = 10$  s can be surveyed belonging to the final extension of 10%. The corresponding maximum tensile stresses are called initial stresses  $\sigma_m$  and are illustrated in the inset graphs of Figure 8. As can be seen, larger inelastic stresses evolving during deformation decrease with increasing temperature due to the reduction of cross-linking densities. According to Eyring's

TABLE 2: Fitting results obtained by the analysis of the relaxation according to the model description of (15) for ESTANE.

$T_{\text{prog}}$	$G^1$	$G^2$	$\tau^1$	$\tau^2$	$G_{\text{eq}}$	Corel. Coeff. $R^2$
10	0.54	0.10	4.56	893.50	0.36	0.975
30	0.70	0.01	8.01	880.81	0.12	0.983
40	0.51	0.11	16.95	1296.61	0.10	0.985
50	0.24	0.18	102.30	883.42	0.52	0.987
60	0.17	0.21	386.90	7724.80	0.59	0.987

theory [33], this can be related to activation volume, which is the volume of the polymer segment involved in the polymer flow [42]. At temperatures below  $T_g$ , polymer chains are in a kind of frozen-in state, where insufficient thermal energy hinders the rotational and transitional movement of whole chain segments. However, Haward [42] has declared that the activation volume has no physical significance despite having the dimension of volume. By increasing temperature, the thermal energy increases towards the barriers for the considerate segmental movement which results in smaller stress levels during deformation.

According to the results illustrated in Figure 8, the experimental initial stresses  $\sigma_m$  are higher than simulation which might be associated with the nonoptimal master-curve generation. However, for all temperatures a fast relaxation process dominates the initial period of relaxations and then a slow process is characteristic for the further relaxations. Moreover, for temperatures below  $T_g$ , the amount of experimental and simulated relaxation stresses converges to each other very fast and good agreement can be observed. At temperatures above glass transition, aside from  $T = 60^\circ\text{C}$ , the conformity deteriorates slightly. The emerging discrepancies between experimental and simulation results at  $T_{\text{prog}} = 50^\circ\text{C}$  are believed to be based on the fact that this temperature is located in the glass transition range, where main chain segmental motions are activated ( $\alpha$ -relaxation). As long as  $T_g$  exceeds better fits could be again achieved.

On the other hand, another interesting aspect is the kinetics of stress relaxations. Figure 9 shows for five selected temperatures the temporal change of stresses as relative values with respect to  $\sigma_m$  at the beginning of the relaxation. Therefore, the model relaxation process starts with an initial value of 1. By trying to find a suitable mathematical fit, it was clear that a simpler generalized Maxwell-Zener model with only five independent parameters ( $G_{\text{eq}}, G_1, G_2, \tau^1, \tau^2$ ) is thoroughly sufficient. Therefore, the experimental data points were fitted to a five-parameter model with a numerical least error square method. The modified Maxwell-Zener model consists of two Maxwell units and a spring in parallel which represents the long-time elastic behavior of the model. This model has the following function:

$$G(t) = \frac{\sigma(t)}{\varepsilon} = G_{\text{eq}} + G^1 \exp\left(-\frac{t}{\tau^1}\right) + G^2 \exp\left(-\frac{t}{\tau^2}\right). \quad (15)$$

The solid lines in Figure 9 are the obtained fitting curves and the calculated fitting parameters. These fitting parameters are listed in Table 2. As can be seen from Figure 9, the relaxation process can be fitted very well with this model and

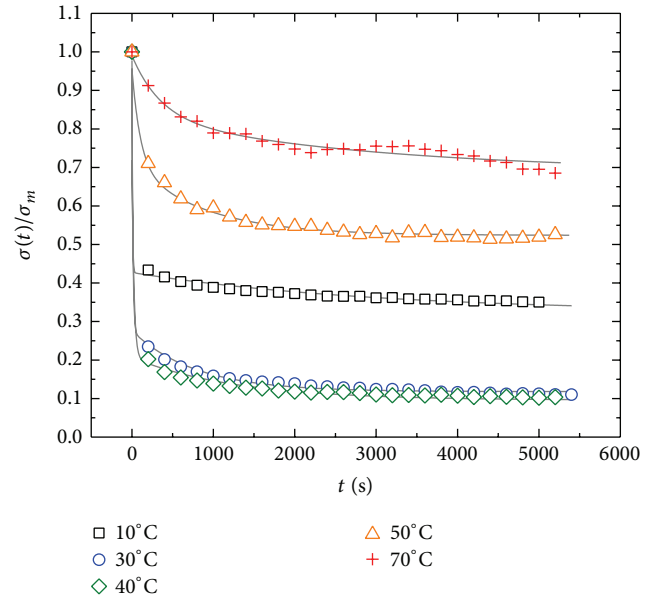


FIGURE 9: Modeling of relaxation curves for ESTANE with the modified Maxwell-Zener model.

the following five unknown parameters at each temperature can be estimated with a good accuracy: the relaxed stress (or the equilibrium stress)  $G_{\text{eq}}$ , the elastic moduli of springs  $G^1$  and  $G^2$ , and relaxation times of dashpots  $\tau^1$  and  $\tau^2$ .

According to the results listed in Table 2 and the fitting curves in Figure 9, it can be established that the main relaxation times  $\tau^1$  increase with increasing  $T_{\text{prog}}$ , meaning that the first unit of the model relaxes faster than the other one. Since  $G^1$  is the dominant spring modulus in the model and because it decreases with temperature,  $\tau^1$  increases proportional to the temperature. Finally, at temperatures below  $T_g$ ,  $G_{\text{eq}}$  decreases with increasing temperature as presented in [43] and then increases to higher values for temperatures higher than glass transition.

#### 4. Conclusion

Based on the Dynamic Mechanical Thermal Analysis and quasistatic experiments, the thermorheological properties of little known ESTANE have been investigated. According to the results presented here, it was possible to estimate its Coefficient of Thermal Expansion above and below glass transition temperature. Consistent with large force fluctuations in tension machine during CTE-determination, it is

believed that the measured CTE from the rheometer test is more reliable. Furthermore, it could be shown that the linear viscoelastic region of ESTANE lay in the range of 0.03 to 1%, which is wider than normally measured with DMTA. As maintained by temperature sweep tests, the glass transition temperature of ESTANE could be measured as the minimum of the  $G'$ - $T$ -graph and is equal to approximately 55°C.

Additionally, it could be shown that the dynamic and out-of-phase viscosities depend strongly on frequency and ESTANE shows a typical more internal energy dominated behavior at lower frequencies. In one step further based on Time-Temperature Superposition Principle, the long-time behavior of ESTANE could be described. A generalized Maxwell model consisting of 19 Maxwell units was then applied to model the viscoelastic behavior of ESTANE. Moreover, relaxation experiments were performed for validating the optimized Prony coefficients. It was observed that at temperatures below  $T_g$ , the experimental data obtained in relaxation experiments coincide better with simulations. In one step further it was revealed that the relaxation results in two steps, one fast and one slow. Since the slower process decays only after some minutes, the relaxation model could be simplified to a five-parameter model.

Finally, in the line of this work, a better understanding about the relaxation kinetics of ESTANE could be achieved. Based on this work we anticipate that these results might provide a necessary knowledge base for further progresses in the development of Shape-Memory Polymers and motivate further studies addressing the particular parameters influencing the kinetics of relaxations.

## Competing Interests

The authors declare no competing interests.

## Acknowledgments

Ehsan Ghobadi and Holger Steeb are grateful to German Science Foundation for the financial support with the DFG Priority Program SPP 1713 "Chemomechanics" (Grant Project no. STE 969/8-1). The authors thank R. Kazakeviciute-Makovska, A. Marquardt, F. Varnik, and G. Eggeler, Ruhr-University Bochum, for sample preparation, injection molding, and valuable discussions.

## References

- [1] M. Behl, J. Zotzmann, and A. Lendlein, "Shape-memory polymers and shape-changing polymers," in *Shape-Memory Polymers*, vol. 226 of *Advances in Polymer Science*, pp. 1–40, Springer, 2010.
- [2] L. Sun, W. M. Huang, Z. Ding et al., "Stimulus-responsive shape memory materials: a review," *Materials and Design*, vol. 33, no. 1, pp. 577–640, 2012.
- [3] W. M. Huang, Y. Zhao, C. C. Wang et al., "Thermo/chemo-responsive shape memory effect in polymers: a sketch of working mechanisms, fundamentals and optimization," *Journal of Polymer Research*, vol. 19, no. 9, pp. 9952–9986, 2012.
- [4] P. T. Mather, X. Luo, and I. A. Rousseau, "Shape memory polymer research," *Annual Review of Materials Research*, vol. 39, no. 1, pp. 445–471, 2009.
- [5] M. Heuchel, T. Sauter, K. Kratz, and A. Lendlein, "Thermally induced shape-memory effects in polymers: quantification and related modeling approaches," *Journal of Polymer Science, Part B: Polymer Physics*, vol. 51, no. 8, pp. 621–637, 2013.
- [6] T. Sauter, M. Heuchel, K. Kratz, and K. A. Lendlein, "Quantifying the shape-memory effect of polymers by cyclic thermomechanical tests," *Polymer Reviews*, vol. 53, no. 1, pp. 6–40, 2013.
- [7] Y. Liu, H. Du, L. Liu, and J. Leng, "Shape memory polymers and their composites in aerospace applications: a review," *Smart Materials and Structures*, vol. 23, no. 2, Article ID 023001, 2014.
- [8] W. Yan, L. Fang, U. Noechel, K. Kratz, and A. Lendlein, "Influence of deformation temperature on structural variation and shape-memory effect of a thermoplastic semi-crystalline multiblock copolymer," *Express Polymer Letters*, vol. 9, no. 7, pp. 624–635, 2015.
- [9] E. Ghobadi, M. Heuchel, K. Kratz, and A. Lendlein, "Influence of the addition of water to amorphous switching domains on the simulated shape-memory properties of poly(L-lactide)," *Polymer*, vol. 54, no. 16, pp. 4204–4211, 2013.
- [10] E. Ghobadi, M. Heuchel, K. Kratz, and A. Lendlein, "Atomistic simulation of the shape-memory effect in dry and water swollen poly(*rac*-lactide)-*co*-glycolide] and copolyester urethanes thereof," *Macromolecular Chemistry and Physics*, vol. 215, no. 1, pp. 65–75, 2014.
- [11] E. Ghobadi, R. Sivanapillai, J. Musialak, and H. Steeb, "Thermo-rheological characterization of polyetherurethane: parameter optimization and validation," in *Constitutive Models for Rubbers IX*, B. Marvalova and I. Petrikova, Eds., vol. 1, chapter 24, pp. 157–163, CRC Press, 2015.
- [12] X. Guo, L. Liu, Y. Liu, B. Zhou, and J. Leng, "Constitutive model for a stress- and thermal-induced phase transition in a shape memory polymer," *Smart Materials and Structures*, vol. 23, no. 10, Article ID 105019, 2014.
- [13] B. Atli, F. Gandhi, and G. Karst, "Thermomechanical characterization of shape memory polymers," *Journal of Intelligent Material Systems and Structures*, vol. 20, no. 1, pp. 87–95, 2009.
- [14] H. Tobushi, T. Hashimoto, S. Hayashi, and E. Yamada, "Thermomechanical constitutive modeling in shape memory polymer of polyurethane series," *Journal of Intelligent Material Systems and Structures*, vol. 8, no. 8, pp. 711–718, 1997.
- [15] H. Tobushi, K. Okumura, S. Hayashi, and N. Ito, "Thermomechanical constitutive model of shape memory polymer," *Mechanics of Materials*, vol. 33, no. 10, pp. 545–554, 2001.
- [16] S. Wineman and K. R. Rajgopal, *Mechanical Response of Polymers: An Introduction*, Cambridge University Press, Cambridge, UK, 2000.
- [17] K. K. Westbrook, P. H. Kao, F. Castro, Y. Ding, and H. J. Qi, "A 3D finite deformation constitutive model for amorphous shape memory polymers: a multi-branch modeling approach for nonequilibrium relaxation processes," *Mechanics of Materials*, vol. 43, no. 12, pp. 853–869, 2011.
- [18] R. Xiao, C. M. Yakacki, J. Guo, C. P. Frick, and T. D. Nguyen, "A predictive parameter for the shape memory behavior of thermoplastic polymers," *Journal of Polymer Science Part B: Polymer Physics*, vol. 54, no. 14, pp. 1405–1414, 2016.
- [19] S. Alexander, R. Xiao, and T. D. Nguyen, "Modeling the thermo-viscoelastic properties and recovery behavior of shape memory polymer composites," *Journal of Applied Mechanics, Transactions ASME*, vol. 81, no. 4, Article ID 041003-1, 2014.

- [20] K. Yu and H. J. Qi, "Temperature memory effect in amorphous shape memory polymers," *Soft Matter*, vol. 10, no. 47, pp. 9423–9432, 2014.
- [21] Q. Ge, X. Luo, C. B. Iversen et al., "A finite deformation thermomechanical constitutive model for triple shape polymeric composites based on dual thermal transitions," *Journal of Applied Mechanics*, vol. 51, no. 15-16, pp. 2777–2790, 2014.
- [22] T. D. Nguyen, "Modeling shape-memory behavior of polymers," *Polymer Reviews*, vol. 53, no. 1, pp. 130–152, 2013.
- [23] Y. Liu, K. Gall, M. L. Dunn, A. R. Greenberg, and J. Diani, "Thermomechanics of shape memory polymers: uniaxial experiments and constitutive modeling," *International Journal of Plasticity*, vol. 22, no. 2, pp. 279–313, 2006.
- [24] T. D. Nguyen, H. J. Qi, F. Castro, and K. N. Long, "A thermoviscoelastic model for amorphous shape memory polymers: incorporating structural and stress relaxation," *Journal of the Mechanics and Physics of Solids*, vol. 56, no. 9, pp. 2792–2814, 2008.
- [25] B. L. Volk, D. C. Lagoudas, and Y.-C. Chen, "Analysis of the finite deformation response of shape memory polymers: II. 1D calibration and numerical implementation of a finite deformation, thermoelastic model," *Smart Materials and Structures*, vol. 19, no. 7, Article ID 075006, 2010.
- [26] R. Kazakeviciute-Makovska, H. Steeb, and A. O. Aydin, "On the evolution law for the frozen fraction in linear theories of shape memory polymers," *Archive of Applied Mechanics*, vol. 82, no. 8, pp. 1103–1115, 2012.
- [27] S. Mogharebi, R. Kazakeviciute-Makovska, H. Steeb, G. Eggeler, and K. Neuking, "On the cyclic material stability of shape memory polymer," *Materialwissenschaft und Werkstofftechnik*, vol. 44, no. 6, pp. 521–526, 2013.
- [28] Anton Paar Germany GmbH, RheoPlus Software. *Software Version: 3.0x*, 2006.
- [29] K. P. Menrad, *Dynamic Mechanical Analysis: A Practical Introduction*, CRC Press, Boca Raton, Fla, USA, 2008.
- [30] R. Kazakeviciūtė-Makovska, A. Özlem Özarmut, and H. Steeb, "Characterization of shape memory polymer estane by means of dynamic mechanical thermal analysis technique," *Smart Materials Research*, vol. 2014, Article ID 250258, 9 pages, 2014.
- [31] C. Liu, H. Qin, and P. T. Mather, "Review of progress in shape-memory polymers," *Journal of Materials Chemistry*, vol. 17, no. 16, pp. 1543–1558, 2007.
- [32] J. D. Menczel and R. B. Prime, *Thermal Analysis of Polymers: Fundamentals and Applications*, John Wiley & Sons, 1st edition, 2009.
- [33] L. H. Sperling, *Introduction to Physical Polymer Science*, Wiley, New York, NY, USA, 4th edition, 2006.
- [34] S. S. Es-Haghi, A. A. Yousefi, and A. Oromiehie, "Thermorheological complexity of poly(methyl methacrylate)/poly(vinylidene fluoride) miscible polymer blend: terminal and segmental levels," *Journal of Polymer Science, Part B: Polymer Physics*, vol. 45, no. 20, pp. 2860–2870, 2007.
- [35] N. A. Hardikar, S. Bobba, and R. Jha, "Applicability of time temperature superposition principle to an immiscible blend of polyphenyleneoxide and polyamide," *Journal of Polymer Engineering*, vol. 31, no. 2-3, pp. 223–236, 2011.
- [36] J. J. Aklonis, W. J. Mac Knight, and M. Shen, *Introduction to Polymer Viscoelasticity: A Practical Introduction*, John Wiley & Sons, New York, NY, USA, 1972.
- [37] J. Weese, "A regularization method for nonlinear ill-posed problems," *Computer Physics Communications*, vol. 77, no. 3, pp. 429–440, 1993.
- [38] P. Haupt, *Continuum Mechanics and Theory of Materials*, Springer, Berlin, Germany, 1999.
- [39] G. A. Holzapfel, *Nonlinear Solid Mechanics: A Continuum Approach for Engineering*, John Wiley & Sons, Chichester, UK, 2000.
- [40] M. Jöhrlitz, H. Steeb, S. Diebels, A. Chatzouridou, J. Batal, and W. Possart, "Experimental and theoretical investigation of nonlinear viscoelastic polyurethane systems," *Journal of Materials Science*, vol. 42, no. 23, pp. 9894–9904, 2007.
- [41] A. V. Shutov, R. Landgraf, and J. Ihlemann, "An explicit solution for implicit time stepping in multiplicative finite strain viscoelasticity," *Computer Methods in Applied Mechanics and Engineering*, vol. 265, pp. 213–225, 2013.
- [42] R. N. Haward, *The Physics of Glassy Polymers*, Springer Science, New York, NY, USA, 2nd edition, 2012.
- [43] M. Heuchel, J. Cui, K. Kratz, H. Kosmella, and A. Lendlein, "Relaxation based modeling of tunable shape recovery kinetics observed under isothermal conditions for amorphous shape-memory polymers," *Polymer*, vol. 51, no. 26, pp. 6212–6218, 2010.



**Hindawi**

Submit your manuscripts at  
<http://www.hindawi.com>

